



Designing the composition and optimizing the mechanical properties of non-equiautomic FeCoNiTi high-entropy alloys

Wei Li^a, Qing Gao^a, Junqiang Ren^{a,*}, Qi Wang^{b, **}, Junchen Li^a, Hongtao Xue^a, Xuefeng Lu^a, Fuling Tang^a

^a State Key Laboratory of Advanced Processing and Recycling of Non-ferrous Metals, School of Materials Science and Engineering, Lanzhou University of Technology, Lanzhou, 730050, China

^b College of Energy Engineering, Huanghuai University, Zhumadian, 463000, China



ARTICLE INFO

Keywords:

HEAs
Molecular dynamics
Elastic modulus
GSFE
Strength-plasticity

ABSTRACT

Research into new high-entropy alloys (HEAs) holds significant promise for advancing aerospace materials. Nevertheless, the complexity of their composition presents formidable challenges in designing HEAs with both high strength and plasticity. In this study, molecular dynamics (MD) simulation was used to explore the optimal composition combination of FeCoNiTi high-entropy alloys with non-equiautomic ratios. Shear modulus (G) characterizes strength, while stacking fault energy (SFE) characterizes plasticity and ductility. Through molecular dynamics (MD) simulations, elastic constants (C11, C12, and C44) and generalized stacking fault energies (GSFEs) for 18 alloy variants were computed. Additionally, the elastic modulus (G, E, and B) for all components was estimated using the Voigt–Reuss–Hill (VRH) averaging method. Following standard guidelines, the composition for the FeCoNiTi alloy was predicted as Ni: 30%–60%, Co: 30%–50%, Fe: 5%–10%, and Ti: 5%–10%. Subsequently, five optimized variants underwent tensile calculations to identify the most suitable composition. The results indicate that the Fe0.05Co0.4Ni0.5Ti0.05 HEA exhibits the best combination of strength and plasticity. Microscopically, its enhanced plasticity is attributed to the twinning-induced plasticity (TWIP) effect. While Fe0.1Co0.4Ni0.4Ti0.1 HEA does not outperform the other variants, it displays a martensitic transformation and deformation twins with increased strain, which are mechanisms not observed in other components. The study of non-equiautomic FeCoNiTi HEAs offers a theoretical foundation for future alloy development. This innovative alloy design method fosters the rapid development of high-performance HEAs, facilitating their rapid development and application.

1. Introduction

High entropy alloys (HEAs) are multi-element alloys [1] characterized by the presence of four or more elements with roughly equal atomic ratios. They typically exhibit a single solid solution structure, such as face-centered cubic (FCC) [2], body-centered cubic (BCC) [3], or close-packed hexagonal (HCP) [4]. Compared to traditional alloys, HEAs offer exceptional properties, including high strength, excellent wear resistance, corrosion resistance, and oxidation resistance, making them widely applicable across various industries. A long-standing challenge in materials research is the trade-off between material strength and plasticity [5,6]. Previous studies have shown that single-phase FCC HEAs often possess excellent plasticity but low strength [7], whereas

single-phase BCC HEAs exhibit high strength but limited plastic deformation ability [8]. To address this, a novel approach has emerged in recent years—designing dual-phase FCC + BCC HEAs to achieve a balance between strength and plasticity. For instance, the AlCoCrFeNi dual-phase HEA demonstrates high strength and ductility, albeit with a more complex deformation mechanism compared to single-phase FCC HEAs [9]. Similarly, Jumaev et al. [10] removed the element Fe and developed an AlCoCrNi dual-phase HEA with low density and excellent mechanical properties. This dual-phase structure comprises a Cr-rich A2 phase and a Ni (Co)-Al B2 phase. The non-stoichiometric composition between Ni and Al in the B2 phase differs from the stoichiometric Ni-Al B2 phase observed in the dual-phase AlCoCrFeNi HEA, highlighting the significant influence of HEA composition and content on dual-phase

* Corresponding author.

** Corresponding author.

E-mail addresses: shrekren520@126.com (J. Ren), wangqi609@163.com (Q. Wang).

HEAs. In this context, customizing the composition and atomic ratios of alloys through alloy design emerges as an effective approach for enhancing the mechanical properties of HEAs.

Fe, Co, and Ni are among the most commonly used matrix elements in HEAs, with FeCoNi often regarded as a medium-entropy alloy. For instance, Watanabe et al. [11] successfully produced a 0.2-mm-thick equiautomic FeCoNi medium-entropy alloy via electrodeposition, featuring a grain size of 10 nm. Tensile experiments revealed a maximum tensile strength of 1.6 GPa, although the elongation was comparatively limited. Ti is frequently used as an alloying element because of its lightweight nature, excellent toughness, and corrosion resistance. To harness these advantages, Chen et al. [12] introduced a small amount of Ti to an intermediate-entropy alloy, namely FeCoNi. After appropriate heat treatment, the yield strength of the resulting $(\text{FeCoNi})_{94}\text{Ti}_6$ intermediate-entropy alloy surged to 893 MPa, the ultimate tensile strength rose to 1263 MPa, and the elongation increased to 24 %, achieving a compelling balance between strength and ductility. As HEAs continued to evolve, FeCoNiTi, a four-element HEA, gained prominence. Liu et al. [13] prepared FeCoNiTi HEA materials with equal atomic ratios using vacuum arc melting and subsequent heat treatment. Their investigations revealed that FeCoNiTi HEA with equal atomic ratios consists of both Laves phases [14] and FCC phases, offering exceptional overall mechanical properties at room temperature. The larger atomic radius of Ti compared to the other three elements enhances its affinity with them, particularly with Fe. This suggests a hypothesis: when Fe and Ti bond, the likelihood of Ti bonding with the other two elements diminishes, leading to an unevenness in the composition of the alloy. Moreover, recent advances in alloy composition have transitioned from equal atomic ratios to non-equal atomic ratios, fostering innovation in HEAs and expanding the potential for high-performance materials [15,16]. As a relatively new HEA, FeCoNiTi has thus far been predominantly studied with equal atomic ratios. This leads to two pertinent questions: (1) Is there a stable structure for non-equal atomic ratios that can yield an improved balance of strength and plasticity? (2) How can composition design and optimization be achieved, considering the known deformation mechanisms, to enhance the strength–plasticity combination in FeCoNiTi HEA?

Designing and optimizing material composition through experimental methods often demands substantial human resources, materials, and financial investments. Computational materials science, an interdisciplinary discipline, focuses on computer simulations and the design of material composition, structure, and properties. Currently, prominent calculation methods include first-principles calculations [17], molecular dynamics (MD) simulations [18], machine learning techniques [19], and finite element calculations [20]. These approaches are favored for their cost-effectiveness in studying material composition design, mechanical properties, and deformation mechanisms. In contrast, MD serves as an atomic-scale calculation tool, offering ease of use and high flexibility. Its simulation methodology, grounded in physical principles, boasts high interpretability and predictability. Consequently, it represents a favorable approach for studying material mechanical properties and determining compositions. For instance, Rao et al. [21] were the first to employ MD simulations to investigate the behavior of $a/2<110>$ dislocations in FCC-structured $\text{Co}_{30}\text{Fe}_{16.67}\text{Ni}_{36.67}\text{Ti}_{16.67}$ alloys. Their findings underscored the significant influence of local composition fluctuations on the activation energy of screw dislocation cross-slip in these alloys. Subsequently, Niu et al. [22] utilized a MC (Monte Carlo) + MD method to explore the impact of chemical short-range order on $\text{Co}_{30}\text{Fe}_{16.67}\text{Ni}_{36.67}\text{Ti}_{16.67}$ HEA. Their results revealed strong local ordering between Fe and Ti, leading to tensile behavior along various crystal orientations. Importantly, the deformation mechanism of $\text{Co}_{30}\text{Fe}_{16.67}\text{Ni}_{36.67}\text{Ti}_{16.67}$ HEA differed significantly depending on the direction. In the [001] direction, it involved an FCC to BCC phase transition, while the [110] and [111] directions featured the generation and movement of Shockley dislocations. Their conclusion suggested that the local chemical ordering simultaneously enhances the strength and

ductility of $\text{Co}_{30}\text{Fe}_{16.67}\text{Ni}_{36.67}\text{Ti}_{16.67}$ HEA. MD simulations can accurately predict the lattice constants [23], generalized fault energies (GSFEs) [24], shear moduli (G) [25], and deformation mechanisms [26] of HEAs. Previous studies have demonstrated that in FCC HEAs, local deformation mechanisms tend to exhibit a strong dependence on SFE [27], whereas G significantly influences the energy barrier and yield strength of dislocation initiation [28].

Previous observations have indicated that Fe and Ti exhibit a strong affinity, imparting a strengthening effect to FeCoNiTi HEA [13,17]. Consequently, this study aims to maintain an equal atomic ratio of Fe and Ti while varying the Ni content to adjust the proportions in other alloy variants., and the shear modulus (G) and the stacking fault energy (γ_{SFE}) of different components are calculated. The identification of the optimal composition serves as a foundational step toward the development of new HEAs featuring non-equal atomic ratios.

2. Simulation method

2.1. Model construction

The EAM potential function has been proved to be a good description of the interaction between metal atoms. In this study, the lattice constants of the selected alloy variants (as shown in Table 1) were determined by LAMMPS software [29] using the Fe–Co–Ni–Ti four-element atomic potential developed by Zhou et al. [30]. A cubic model measuring $18 \text{ \AA} \times 18 \text{ \AA} \times 18 \text{ \AA}$ was established with FCC Ni as the matrix element. The Fe, Co, and Ti atoms were substituted according to specified contents to obtain different lattice constants. Subsequently, a new model was constructed based on the measured lattice constants. This new model also used Ni as the matrix, with other atom types being replaced according to specifications, maintaining the same model size of $18 \text{ \AA} \times 18 \text{ \AA} \times 18 \text{ \AA}$. The elastic constants C_{11} , C_{12} , and C_{44} of FeCoNiTi HEA were calculated based on linear elasticity theory, and the bulk modulus (B), shear modulus (G), Young's modulus (E), and Poisson's ratio (v) were calculated according to the respective formulas.

The calculation process for the GSFE is depicted in Fig. 1. Model dimensions were defined based on lattice constants corresponding to the various alloy variants. The x, y, and z axes were oriented along [112], $[\bar{1}10]$, and $[1\bar{1}1]$, respectively. Periodic boundary conditions were applied to the x and y axes, while free boundary conditions were used for the z axis. The model was divided into two parts, with the lower portion fixed and the upper portion allowed to slide along (111) in the direction [112]. The total displacement for each slip corresponds to the length of a Burgers vector (\mathbf{b}_v), defined as $\mathbf{b}_v = a_0/6<112>$, where a_0 represents the

Table 1
Composition of FeCoNiTi HEAs.

Type	Alloys
(A) $\frac{\text{Fe}_{(0.8-x)}\text{Co}_x\text{Ni}_{0.2}\text{Ti}_{(0.8-x)}}{2}$	(1) $\text{Fe}_{0.3}\text{Co}_{0.2}\text{Ni}_{0.2}\text{Ti}_{0.3}$ (2) $\text{Fe}_{0.25}\text{Co}_{0.3}\text{Ni}_{0.2}\text{Ti}_{0.25}$ (3) $\text{Fe}_{0.2}\text{Co}_{0.4}\text{Ni}_{0.2}\text{Ti}_{0.2}$ (4) $\text{Fe}_{0.15}\text{Co}_{0.5}\text{Ni}_{0.2}\text{Ti}_{0.15}$ (5) $\text{Fe}_{0.25}\text{Co}_{0.2}\text{Ni}_{0.3}\text{Ti}_{0.25}$ (6) $\text{Fe}_{0.2}\text{Co}_{0.3}\text{Ni}_{0.3}\text{Ti}_{0.2}$ (7) $\text{Fe}_{0.15}\text{Co}_{0.4}\text{Ni}_{0.3}\text{Ti}_{0.15}$ (8) $\text{Fe}_{0.1}\text{Co}_{0.5}\text{Ni}_{0.3}\text{Ti}_{0.1}$ (9) $\text{Fe}_{0.2}\text{Co}_{0.2}\text{Ni}_{0.4}\text{Ti}_{0.2}$ (10) $\text{Fe}_{0.15}\text{Co}_{0.3}\text{Ni}_{0.4}\text{Ti}_{0.15}$ (11) $\text{Fe}_{0.1}\text{Co}_{0.4}\text{Ni}_{0.4}\text{Ti}_{0.1}$ (12) $\text{Fe}_{0.05}\text{Co}_{0.5}\text{Ni}_{0.4}\text{Ti}_{0.05}$ (13) $\text{Fe}_{0.15}\text{Co}_{0.2}\text{Ni}_{0.5}\text{Ti}_{0.15}$ (14) $\text{Fe}_{0.1}\text{Co}_{0.3}\text{Ni}_{0.5}\text{Ti}_{0.1}$ (15) $\text{Fe}_{0.05}\text{Co}_{0.4}\text{Ni}_{0.5}\text{Ti}_{0.05}$ (16) $\text{Fe}_{0.1}\text{Co}_{0.2}\text{Ni}_{0.6}\text{Ti}_{0.1}$ (17) $\text{Fe}_{0.05}\text{Co}_{0.3}\text{Ni}_{0.6}\text{Ti}_{0.05}$ (18) $\text{Fe}_{0.05}\text{Co}_{0.2}\text{Ni}_{0.7}\text{Ti}_{0.05}$
(B) $\frac{\text{Fe}_{(0.8-x)}\text{Co}_x\text{Ni}_{0.3}\text{Ti}_{(0.8-x)}}{2}$	
(C) $\frac{\text{Fe}_{(0.8-x)}\text{Co}_x\text{Ni}_{0.4}\text{Ti}_{(0.8-x)}}{2}$	
(D) $\frac{\text{Fe}_{(0.8-x)}\text{Co}_x\text{Ni}_{0.5}\text{Ti}_{(0.8-x)}}{2}$	
(E) $\frac{\text{Fe}_{(0.8-x)}\text{Co}_x\text{Ni}_{0.6}\text{Ti}_{(0.8-x)}}{2}$	
(F) $\frac{\text{Fe}_{(0.8-x)}\text{Co}_x\text{Ni}_{0.7}\text{Ti}_{(0.8-x)}}{2}$	

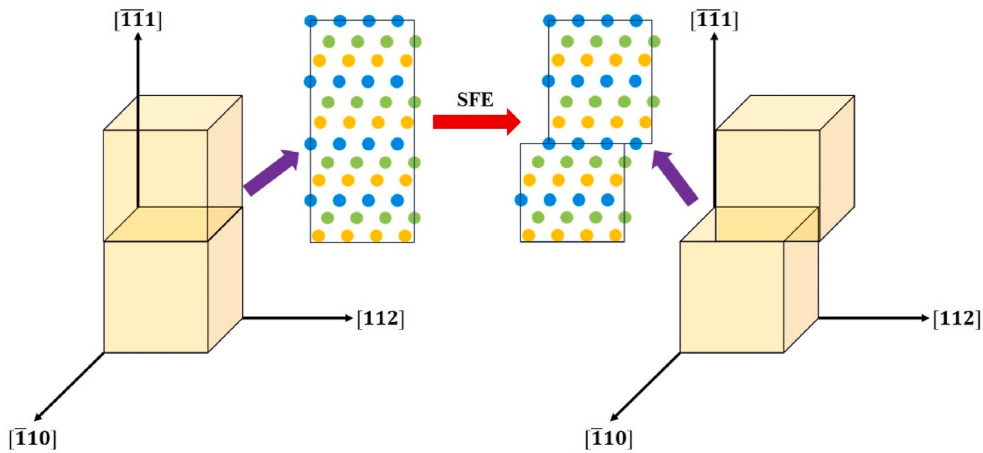


Fig. 1. Schematic of GSFE calculation and the upper and lower portions of the relative slip model.

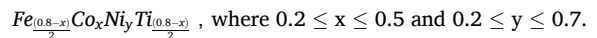
lattice constant. A displacement of one \mathbf{b}_v results in the creation of an intrinsic stacking fault (ISF), while a two- \mathbf{b}_v displacement leads to the formation of an extrinsic stacking fault (ESF). A three- \mathbf{b}_v displacement produces deformation twins. The stacking fault energy (SFE) after defects have formed was calculated using the formula $E = (E_f - E_0)/A$, where E_f signifies the energy after the formation of the stacking fault, E_0 represents the initial energy of the system, and A denotes the area of the slip plane.

Based on the calculated lattice constants and elastic moduli, variants displaying elastic instability were excluded. Additionally, those with relatively high ISF values were removed based on the GSFE. The average values of G and ISF were calculated for the remaining variants. We selected variants that had values greater than the average G and less than the average ISF. The intersection of these variants yielded our final predicted composition. Subsequently, uniaxial tensile loading was performed on HEAs with this final composition. The tests were conducted at a temperature of 300 K and a tensile rate of $1 \times 10^8 \text{ s}^{-1}$. We analyzed the mechanical properties and deformation mechanisms to identify the alloy variant that offered the best combination of strength and plasticity.

2.2. Definition criteria

Prior studies have demonstrated that dislocation slip [31], TWIP [32], and transformation-induced plasticity (TRIP) [33] are the primary deformation mechanisms in FCC HEAs. A reduction in SFE generally leads to a transition from dislocation slip to TWIP or TRIP, significantly improving the strength and ductility of FCC HEAs [34]. Recent research has also indicated that altering the alloy composition reduces SFE [35], triggering TWIP or TRIP mechanisms to achieve a superior strength–plasticity balance in HEAs. It is important to note that yield strength is not directly related to TWIP or TRIP mechanisms, as both mechanisms occur during the plastic deformation stage. For FCC HEAs, the elastic modulus plays a central role in determining material properties. Notably, the elastic modulus dictates the stress–strain relationship in the elastic stage. The shear modulus (G) is closely related to dislocation motion in the slip plane, with the Peierls stress required for dislocation slip being proportional to G [36]. This underscores the significance of G in evaluating the yield strength of HEAs.

Consequently, a standard can be defined based on GSFE and G to characterize the plasticity and strength of FeCoNiTi HEA, respectively. Specifically, a low GSFE and high G indicate a desirable combination of strength and plasticity for the HEA. Thus, to select the composition of FeCoNiTi HEA with the best strength–plasticity balance and to understand the influence of alloy variant composition on mechanical properties, this study uses G and GSFE to assess the strength and plasticity of the alloys. The selected composition is represented as



3. Results and discussions

3.1. Lattice parameters

The final composition was determined based on 18 different combinations with Fe: 0.05–0.3, Co: 0.2–0.5, Ni: 0.2–0.7, and Ti: 0.05–0.3. The correlation between the lattice constant and Ni content is shown in Fig. 2. As Ni content increases, the lattice constant exhibits a declining trend. This trend can be primarily attributed to the elevation of Ni content leading to reduced lattice distortion, aligning the lattice closer to the (pure Ni) lattice structure of the matrix. When the Ni content remains constant, a similar declining trend is observed in the lattice constant with the increasing Co content. Notably, the minimum lattice constant is observed in $\text{Fe}_{0.05}\text{Co}_{0.2}\text{Ni}_{0.7}\text{Ti}_{0.05}$, measuring 3.556 \AA , while the maximum is found in $\text{Fe}_{0.3}\text{Co}_{0.2}\text{Ni}_{0.2}\text{Ti}_{0.3}$, measuring 3.73 \AA . The difference between these two extremes amounts to 0.174 \AA , and it is noteworthy that both the maximum and minimum values surpass the lattice constant of pure Ni (3.52 \AA). This observation underscores that the addition of Fe, Co, and Ti atoms induces significant lattice distortion, a hallmark characteristic of HEAs [37]. In the previous study of FeCoNiTi high-entropy alloy, Liu et al. [13] designed FeCoNiTi with equal

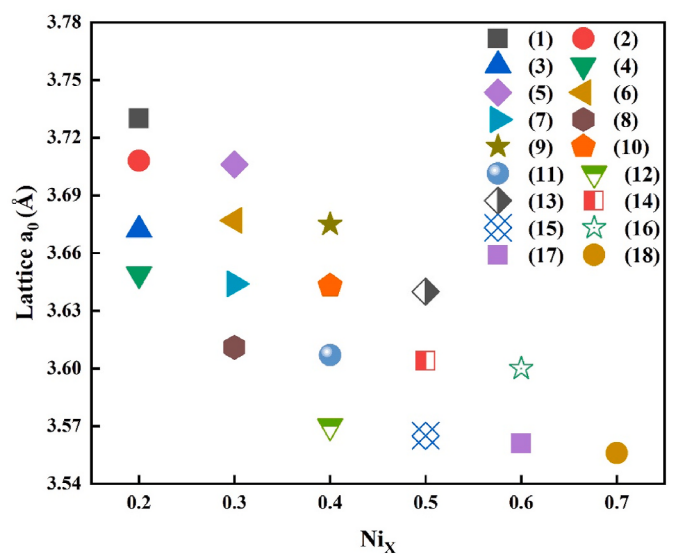


Fig. 2. Dependence of lattice constant on Ni content.

atomic ratio by experiments. The results show that the addition of Ti atoms is easy to bond with the other three elements. The higher the atomic size mismatch of the alloying elements, the stronger the solid solution strengthening effect of the alloy. The Young's modulus mismatch between Fe and Ti is as high as 81.9 %, which further enhances the solid solution strengthening effect. At the same time, Niu et al. [23] conducted MC + MD simulations on FeCoNiTi high-entropy alloys with non-equivalent atomic ratios. The results show that Fe-Ti atomic pairs are most likely to form local ordered structures. Therefore, maintaining the same content of Fe and Ti elements, the influence of Ni content changes on mechanical properties and deformation mechanisms was analyzed.

In order to explore the root cause of the phenomenon of increasing the content of Ni and Co, reducing the content of Fe and Ti, and reducing the lattice constant, the first-principles were used to study. First use MS to carry out first-principles research, and established two alloy models. The content 1 is $\text{Fe}_{0.15}\text{Co}_{0.3}\text{Ni}_{0.4}\text{Ti}_{0.15}$, and the content 2 is $\text{Fe}_{0.05}\text{Co}_{0.4}\text{Ni}_{0.5}\text{Ti}_{0.05}$. The two models have 32 atoms each. After calculation, the lattice constant of content 1 is $a_1 = 7.183961 \text{ \AA}$, $b_1 = 7.158701 \text{ \AA}$, and the lattice constant of content 2 is $a_2 = 7.076094 \text{ \AA}$, $b_2 = 7.0679 \text{ \AA}$. Obviously, increasing the content of Ni and Co and decreasing the content of Fe and Ti will reduce the lattice constant. Fig. 3 shows the differential charge diagram of the two components. It can be seen from the figure that the fundamental reason for the increase of lattice constant is the transfer of electrons. The more electrons transfer, the stronger the attraction between atoms, which leads to the decrease of lattice constant.

3.2. Mechanical properties

The calculated elastic constants C_{11} , C_{12} , and C_{44} for each variant are presented in Table 2. Using these elastic constants, we approximated B , E , G , and v via the Voigt-Reuss-Hill (VRH) averaging method [38]. The specific formulae are given as equations (1)–(6), and the calculated results are depicted in Fig. 4(b) and (d). B reflects the bond strength between atoms and resistance to cracking, E reflects the rigidity of the material, while the shear modulus (G) characterizes resistance to dislocation motion. Typically, v falls within the range of 0.26–0.5.

$$B = \frac{(C_{11} + 2C_{12})}{3} \quad (1)$$

$$G_V = \frac{(C_{11} - C_{12}) + 3C_{44}}{5} \quad (2)$$

$$G_R = \frac{5(C_{11} - C_{12})C_{44}}{3(C_{11} - C_{12}) + 4C_{44}} \quad (3)$$

$$G = \frac{(C_V - C_R)}{2} \quad (4)$$

$$E = \frac{9BG}{3B + G} \quad (5)$$

$$v = \frac{(3B - 2G)}{6B + 2G} \quad (6)$$

Based on the aforementioned elastic constants, we can calculate C' and Cauchy pressure C_P , and the computed results are presented in Fig. 4 (b). The calculation formula is as follows:

$$C' = \frac{(C_{11} - C_{12})}{2} \quad (7)$$

$$C_P = C_{11} - C_{44} \quad (8)$$

Here, C' is used to characterize mechanical stability [21]. C_P , on the other hand, indicates the balance between covalent and metal bonding in the material. When $C_P > 0$, metal bonds dominate, leading to increased plasticity. Conversely, when $C_P < 0$, covalent bonds dominate, resulting in high strength and hardness.

Fig. 4 presents the elastic properties of the various variants. In particular, Fig. 4(a) illustrates the variation in elastic constants C_{11} , C_{12} , and C_{44} as the Ni and Co contents increase. With rising Ni and Co contents, C_{11} exhibits a monotonically increasing trend, though its minimum value occurs in variant 6 ($\text{Fe}_{0.2}\text{Co}_{0.3}\text{Ni}_{0.3}\text{Ti}_{0.2}$). C_{12} and C_{44} , on the whole, also display a monotonically increasing trend, albeit with a slight fluctuation in C_{12} in groups A and B. Fig. 4 reveals the behaviors of B , E , and G for each alloy variant. Overall, B , E , and G exhibit a monotonically increasing trend with the increasing Ni and Co contents, but there is an exception in the case of variant 6 ($\text{Fe}_{0.2}\text{Co}_{0.3}\text{Ni}_{0.3}\text{Ti}_{0.2}$). Notably, as the Ni content increases from 0.2 to 0.7, G escalates from 5.26 GPa to 38.17 GPa. Based on the calculations, in group A, as the Co content rises, the Fe and Ti contents decrease, resulting in a 90.11 % increase in G . Data outliers in group B were not computed. Groups C, D, and E exhibited 137.6 %, 64.86 %, and 25.29 % enhancements in G , respectively. In summary, the increase in G , stemming from higher Ni and Co content and the reduction of Fe and Ti content, contributes to increased Peierls stress and yield strength (refer to Section 2).

Fig. 4(c) displays the values of C' and C_P for each alloy variant. Specifically, variant 6 exhibits a negative C' value, signifying that $\text{Fe}_{0.2}\text{Co}_{0.3}\text{Ni}_{0.3}\text{Ti}_{0.2}$ is mechanically unstable. In contrast, the C_P values for all variants are positive, indicative of the selected components having excellent plasticity. In Fig. 4(d), the Poisson's ratio v for each variant is depicted. Variant 6($\text{Fe}_{0.2}\text{Co}_{0.3}\text{Ni}_{0.3}\text{Ti}_{0.2}$) shows a value exceeding 0.5, while the other components exhibit values ranging from 0.26 to 0.5. This

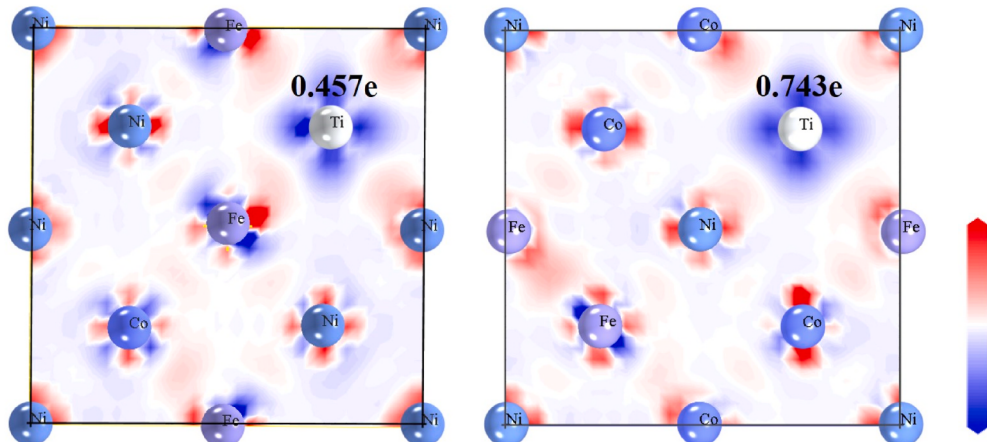
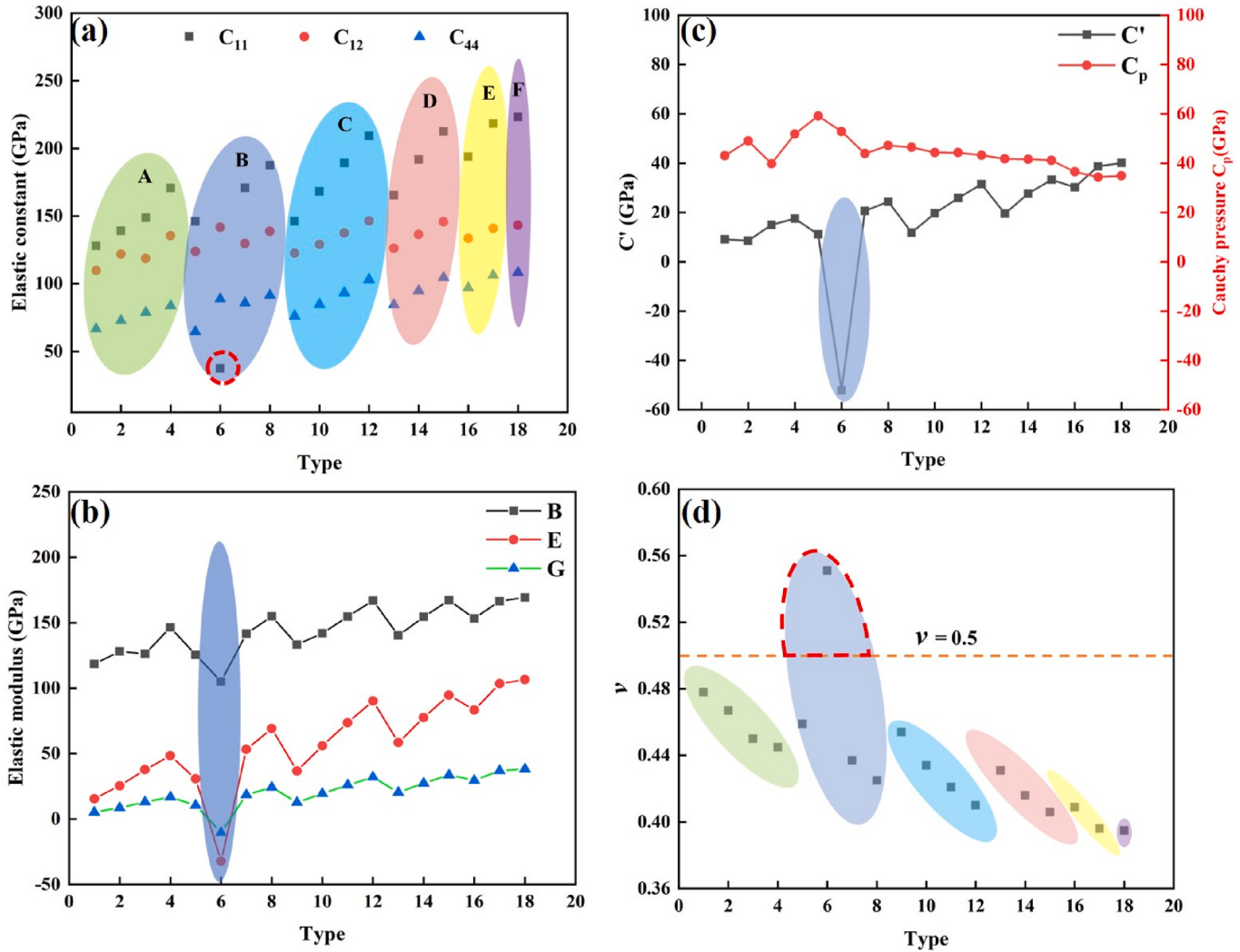


Fig. 3. Differential charge diagram (a) $\text{Fe}_{0.15}\text{Co}_{0.3}\text{Ni}_{0.4}\text{Ti}_{0.15}$, (b) $\text{Fe}_{0.05}\text{Co}_{0.4}\text{Ni}_{0.5}\text{Ti}_{0.05}$.

Table 2 C_{11} , C_{12} , and C_{44} for each variant.

	1	2	3	4	5	6	7	8	9
C_{11}	128	139.06	148.78	170.73	146	37.51	170.93	187.55	146.15
C_{12}	109.76	121.91	118.72	135.59	123.81	141.68	129.76	138.75	122.56
C_{44}	66.72	72.88	78.92	89.77	64.65	88.87	85.87	91.58	76.1
	10	11	12	13	14	15	16	17	18
C_{11}	168.26	189.21	209.35	165.28	191.76	212.38	193.92	218.35	223.37
C_{12}	129.05	137.55	146.34	126.21	136.4	145.73	133.49	140.82	143.18
C_{44}	84.72	93.27	103.1	84.49	94.81	104.57	97.03	106.46	108.33

**Fig. 4.** (a) Elastic constants C_{11} , C_{12} , and C_{44} , (b) Elastic modulus (B, E, G), (c) C' , Cauchy pressure C_p , (d) Poisson's ratio ν .

indirectly suggests that the mechanical properties of component 6 ($(\text{Fe}_{0.2}\text{Co}_{0.3}\text{Ni}_{0.3}\text{Ti}_{0.2})$) are less stable. Additionally, it is observed that both C_p and ν exhibit a decreasing trend with the increase in Co content, indicating that a higher Co content enhances the strength and hardness of the alloy, while maintaining overall excellent plasticity.

3.3. SFE and deformation mechanisms

Fig. 5 illustrates the GSFE resulting from atomic misalignment in the [112] direction. In Fig. 5(a), the representative GSFE curve for metals with an FCC structure is displayed, where green atoms represent the FCC structure, red atoms represent the HCP structure, and the deformation initiates with an ISF, followed by an ESF, and eventually leads to a

deformation twin. Examining the curve, the maximum values represent the energy γ_{UI} required to introduce the ISF, the energy γ_{UE} needed to introduce the ESF, and the energy γ_{UT} required to introduce a deformation twin. The minimum values on the curve represent the energy γ_{ISF} of the intrinsic faults, γ_{ESF} of the extrinsic faults, and γ_{TW} of the deformation twins.

In addition, Fig. 5(b) displays the results for variants 1($\text{Fe}_{0.3}\text{Co}_{0.2}\text{Ni}_{0.2}\text{Ti}_{0.3}$), 2($\text{Fe}_{0.25}\text{Co}_{0.3}\text{Ni}_{0.2}\text{Ti}_{0.25}$), 5($\text{Fe}_{0.25}\text{Co}_{0.2}\text{Ni}_{0.3}\text{Ti}_{0.25}$), 9($\text{Fe}_{0.2}\text{Co}_{0.2}\text{Ni}_{0.4}\text{Ti}_{0.2}$), and 13($\text{Fe}_{0.15}\text{Co}_{0.2}\text{Ni}_{0.5}\text{Ti}_{0.15}$), demonstrating that γ_{ISF} is relatively high, requiring an increased amount of energy to generate ISFs compared to the other variants. With the increase in Co content and decrease in Fe and Ti contents, γ_{ISF} displays a decreasing trend. The red line in the figure indicates that when Co content is 0.2, Fe

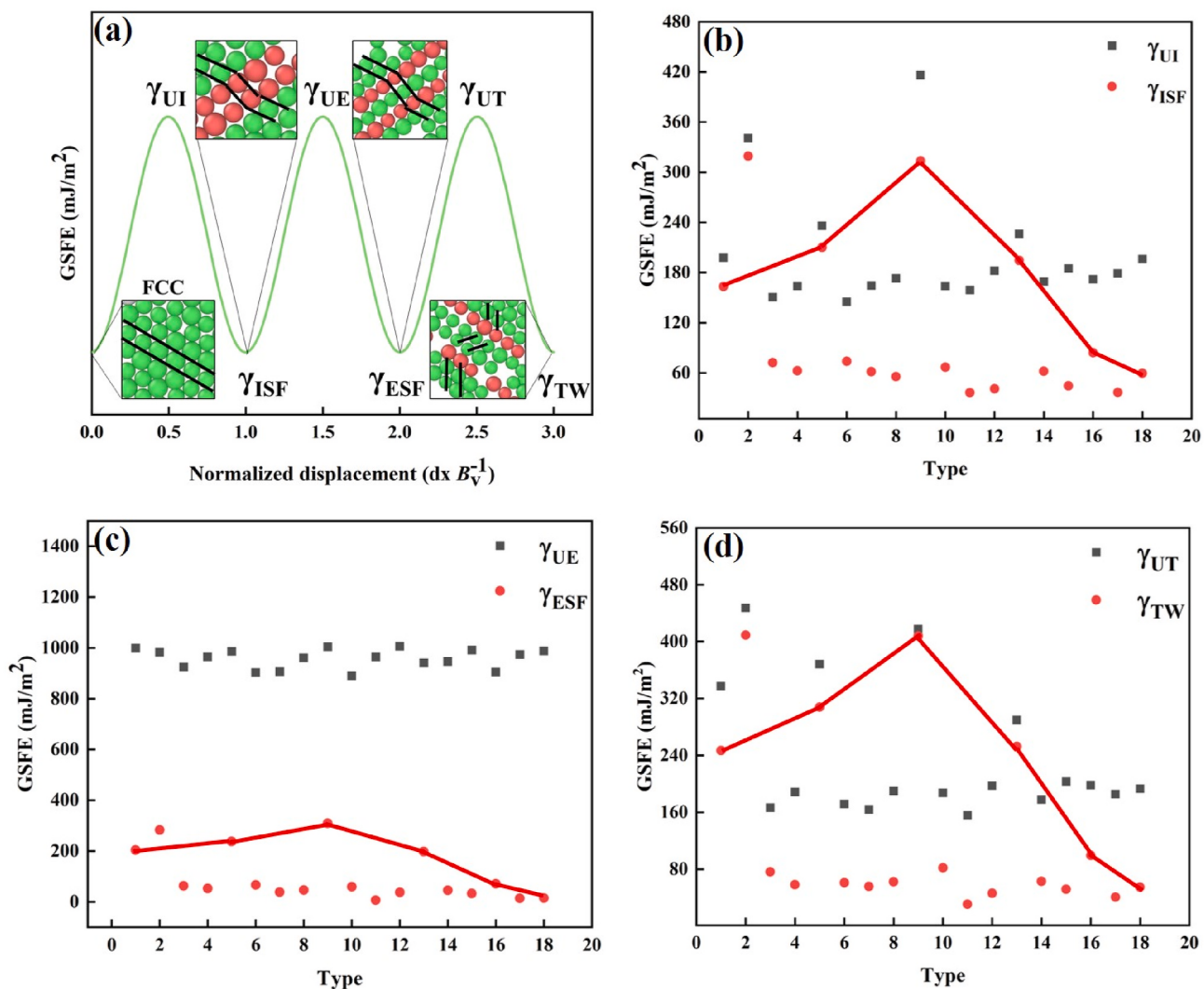


Fig. 5. GSFE of FCC FeCoNiTi HEAs. (a) Standard GSFE curve, (b) γ_{UI} and γ_{ISF} , (c) γ_{UI} and γ_{ESF} , and (d) γ_{UI} and γ_{TW} of the alloy variants.

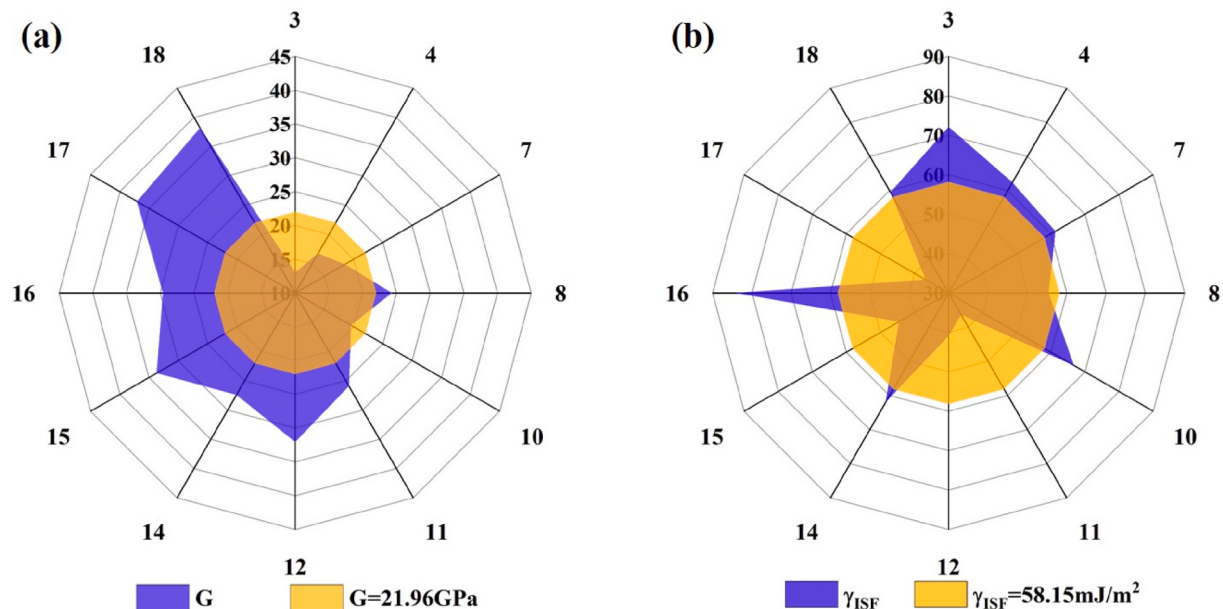


Fig. 6. Optimal composition selection diagram. (a) Selection based on G value, (b) selection based on γ_{ISF} .

and Ti contents decrease as Ni content increases, causing γ_{ISF} to first increase and then decrease. Fig. 5 (a) and (b) also show γ_{ESF} and γ_{TW} for each variant, which exhibit a similar variation pattern to γ_{ISF} . The results reveal that increased Ni and Co contents lead to a reduction in SFE, causing the deformation mechanism to shift from dislocation slip to TWIP. Previous studies have indicated that for FCC HEAs, as SFE decreases further, the primary deformation mechanism changes from TWIP to TRIP. The presence of TWIP or TRIP significantly enhances the strength, work-hardening ability, and ductility of FCC HEAs with lower SFEs. The results presented in Fig. 5 demonstrate that SFE can serve as a criterion to assess the influence of chemical composition content on the deformation mechanism of FCC HEAs.

3.4. Optimal ingredient selection

Figs. 4 and 5 were analyzed to exclude the elastic, unstable variant 6 ($Fe_{0.2}Co_{0.3}Ni_{0.3}Ti_{0.2}$) and the high-GSFE variants 1 ($Fe_{0.3}Co_{0.2}Ni_{0.2}Ti_{0.3}$), 2 ($Fe_{0.25}Co_{0.3}Ni_{0.2}Ti_{0.25}$), 5 ($Fe_{0.25}Co_{0.2}Ni_{0.3}Ti_{0.25}$), 9 ($Fe_{0.2}Co_{0.2}Ni_{0.4}Ti_{0.2}$), and 13 ($Fe_{0.15}Co_{0.2}Ni_{0.5}Ti_{0.15}$), which exhibit limited plastic deformation tendencies. The G and γ_{ISF} values of the remaining variants were averaged, and the variants with G values greater than the mean G value and γ_{ISF} values less than the mean γ_{ISF} value were selected.

Fig. 6(a) illustrates the G values of the remaining variants, where the yellow area represents the average G value and the blue area displays the G value for each variant. Following the criteria, variants exceeding the average G value were selected, resulting in the selection of variants 8 ($Fe_{0.1}Co_{0.5}Ni_{0.3}Ti_{0.1}$), 11 ($Fe_{0.1}Co_{0.4}Ni_{0.4}Ti_{0.1}$), 12 ($Fe_{0.05}Co_{0.5}Ni_{0.4}Ti_{0.05}$), 14 ($Fe_{0.1}Co_{0.3}Ni_{0.5}Ti_{0.1}$), 15 ($Fe_{0.05}Co_{0.4}Ni_{0.5}Ti_{0.05}$), 16 ($Fe_{0.1}Co_{0.2}Ni_{0.6}Ti_{0.1}$), 17 ($Fe_{0.05}Co_{0.3}Ni_{0.6}Ti_{0.05}$), and 18 ($Fe_{0.05}Co_{0.2}Ni_{0.7}Ti_{0.05}$). Fig. 6(b) presents the γ_{ISF} values of the remaining variants, with the yellow area indicating the average γ_{ISF} value and the blue area depicting the γ_{ISF} value for each variant. According to the standard, variants whose γ_{ISF} value is less than the average γ_{ISF} were selected, and this resulted in the selection of variants 8 ($Fe_{0.1}Co_{0.5}Ni_{0.3}Ti_{0.1}$), 11 ($Fe_{0.1}Co_{0.4}Ni_{0.4}Ti_{0.1}$), 12 ($Fe_{0.05}Co_{0.5}Ni_{0.4}Ti_{0.05}$), 15 ($Fe_{0.05}Co_{0.4}Ni_{0.5}Ti_{0.05}$), and 17 ($Fe_{0.05}Co_{0.3}Ni_{0.6}Ti_{0.05}$). Thus, the variants meeting both criteria, namely variants 8 ($Fe_{0.1}Co_{0.5}Ni_{0.3}Ti_{0.1}$), 11 ($Fe_{0.1}Co_{0.4}Ni_{0.4}Ti_{0.1}$), 12 ($Fe_{0.05}Co_{0.5}Ni_{0.4}Ti_{0.05}$), 15 ($Fe_{0.05}Co_{0.4}Ni_{0.5}Ti_{0.05}$), and 17 ($Fe_{0.05}Co_{0.3}Ni_{0.6}Ti_{0.05}$), were chosen, and these exhibit the best performance.

3.5. Tensile properties and dislocation evolution

The five variants selected in the previous section (Section 3.4) were then subjected to tensile experiments to identify the variant with the best performance and validate the selection criteria. The tensile experiments were conducted at a temperature of 300 K and a tensile rate of $1 \times 10^8 s^{-1}$. It is important to note that no defects were present in the constructed simulation unit, resulting in relatively high stress during the tensile process and elevated stress values around the yield point. Despite these variations, the stress-strain curves obtained from MD simulations align well with the trends observed in HEA experiments [39,40]. The stress-strain curves of the five selected variants are presented in Fig. 7.

In this section, the plastic deformation mechanism during tensile process is studied by stress-strain curve, and the dislocation motion, stacking fault transformation and their interaction under different strains are analyzed in detail to explain the reason of stress change. When studying the tensile properties of each component, the tensile parameters are kept consistent to ensure the accuracy of the tensile properties of each component. As for why ignore other factors, this is mainly to reduce the complexity of the simulation. In the research, specific deformation mechanisms or problems are often studied, so other irrelevant factors are ignored to simplify the research object and better understand the influence of key factors on the macroscopic plastic behavior.

Fig. 7 shows the stress-strain curves of the five selected variants. The

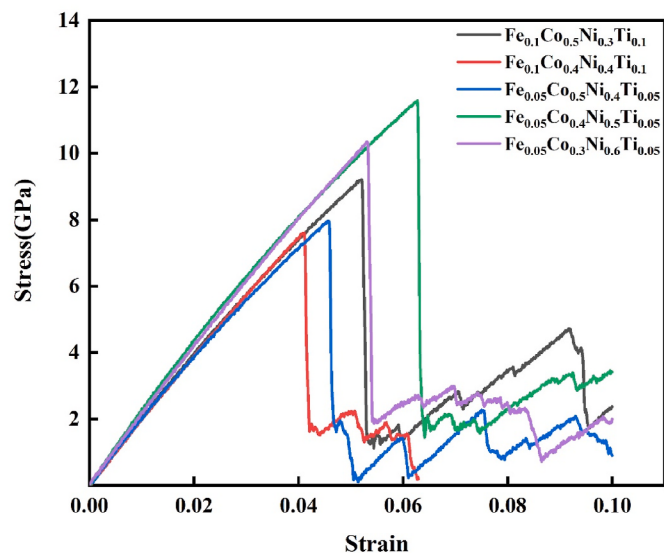


Fig. 7. Stress–strain curves of the five variants.

highest stress corresponds to the yield stress, and the strain at this point is considered the yield strain. Table 3 lists the yield strength (σ_y) and yield strain (ϵ_y) for the five variants. A comparison reveals that variant 15, $Fe_{0.05}Co_{0.4}Ni_{0.5}Ti_{0.05}$ HEA, exhibits the highest yield strength (11.59 GPa) and the highest yield strain (6.3 %). The TRIP mechanism observed in FCC HEAs can be categorized into two types: (1) FCC→HCP and (2) FCC→BCC. The proportion of HCP or BCC phases in HEAs can be used to evaluate the TRIP tendency during the tension process. Additionally, dislocation motion, specifically the Shockley partial dislocation density, can provide insight into the Stacking fault changes.

From Fig. 8(a), it is evident that the HCP structure of all variants initially exhibits an upward trend. When combined with Fig. 8(b), this trend is linked to the movement of Shockley partial dislocations, which are associated with the HCP structure. As strain increases, with the exception of variants 8 ($Fe_{0.1}Co_{0.5}Ni_{0.3}Ti_{0.1}$) and 17 ($Fe_{0.05}Co_{0.3}Ni_{0.6}Ti_{0.05}$), the HCP structure in other variants begins to decline. Subsequently, all variants experience an upward trend, although the rate of increase varies. Notably, in variant 11 ($Fe_{0.1}Co_{0.4}Ni_{0.4}Ti_{0.1}$), the HCP structure disappears at a strain of 6.5 %, indicating a martensitic transition (FCC→BCC transition) under this level of strain. Observing the changes in the HCP structure and Shockley dislocations for each variant (Fig. 8(a) and b), it becomes evident that Shockley dislocations are closely tied to the HCP structure. When the trends of the two parameters follow a similar pattern, it indicates that the HCP structure at that stage is a result of a stacking fault rather than a true HCP phase. Consequently, variants 12 ($Fe_{0.05}Co_{0.5}Ni_{0.4}Ti_{0.05}$) and 17 ($Fe_{0.05}Co_{0.3}Ni_{0.6}Ti_{0.05}$) do not undergo phase transitions, suggesting that the strain is insufficient to induce phase transitions. For variant 8 ($Fe_{0.1}Co_{0.5}Ni_{0.3}Ti_{0.1}$), when the strain reaches 9.45 %, the dislocation density of Shockley dislocations approaches 0. However, the proportion of HCP structure at this stage remains close to 25 %. This suggests that under this strain, the HCP structure no longer results from stacking faults caused by Shockley partial dislocation but rather from an FCC→HCP phase transition. As the

Table 3
Yield strength (σ_y) and yield strain (ϵ_y) of the five variants.

Alloy	Yield strength (GPa)	Yield strain (%)
(8) $Fe_{0.1}Co_{0.5}Ni_{0.3}Ti_{0.1}$	9.21	5.2
(11) $Fe_{0.1}Co_{0.4}Ni_{0.4}Ti_{0.1}$	7.61	4.1
(12) $Fe_{0.05}Co_{0.5}Ni_{0.4}Ti_{0.05}$	7.97	4.6
(15) $Fe_{0.05}Co_{0.4}Ni_{0.5}Ti_{0.05}$	11.59	6.3
(17) $Fe_{0.05}Co_{0.3}Ni_{0.6}Ti_{0.05}$	10.35	5.3

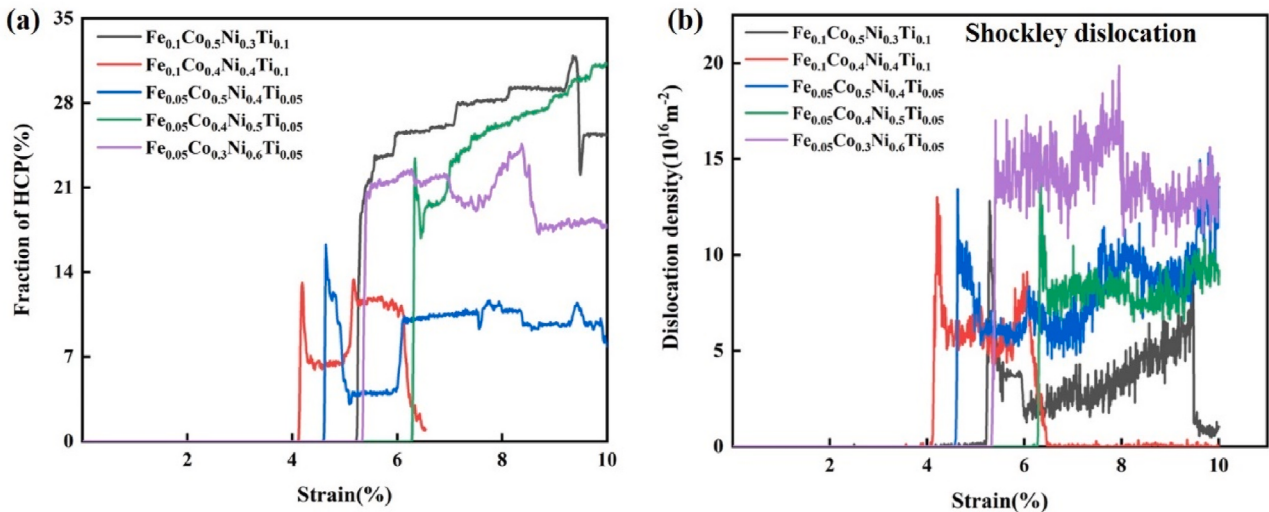


Fig. 8. Phase transition and dislocation density of HEAs during tensile deformation. (a) HCP phase variation and (b) Density of Shockley partial dislocations.

strain continues to increase, the plastic deformation mechanism for these variant transitions from dislocation slip to TRIP.

In contrast to other variants, variant 15($\text{Fe}_{0.05}\text{Co}_{0.4}\text{Ni}_{0.5}\text{Ti}_{0.05}$) exhibits a unique behavior. Up to a strain of 6.5 %, its HCP structure and Shockley dislocations share a similar trend, signifying that dislocations dominate the plastic deformation process during this phase. However, beyond a strain of 6.5 %, the HCP structure continues to increase with strain, while the Shockley dislocations remain relatively stable. This suggests that the increase in HCP structure results from an FCC to HCP phase transition. Overall, variant 15($\text{Fe}_{0.05}\text{Co}_{0.4}\text{Ni}_{0.5}\text{Ti}_{0.05}$), exhibits delayed dislocation nucleation, indicating high strength. It also undergoes the earliest phase transition, signifying good plasticity. As a result, variant 15 ($\text{Fe}_{0.05}\text{Co}_{0.4}\text{Ni}_{0.5}\text{Ti}_{0.05}$) is identified as the optimal variant, with both high strength and plasticity.

3.6. Deformation mechanism evolution

Based on the earlier analysis, it was determined that a 10 % strain is insufficient to induce the TRIP effect in variants 12 ($\text{Fe}_{0.05}\text{Co}_{0.5}\text{Ni}_{0.4}\text{Ti}_{0.05}$) and 17($\text{Fe}_{0.05}\text{Co}_{0.3}\text{Ni}_{0.6}\text{Ti}_{0.05}$). Consequently, the following analysis focuses on the microstructure evolution, including ISF, ESF, FCC to HCP phase transition, FCC to BCC phase transition, deformation twins, and Lomer-Cottrell dislocation locks, of the remaining three variants. During the tensile process, the nucleation and movement of dislocations are the main deformation mechanisms. The interaction

between dislocations produces L-C dislocation locks. The sliding of Shockley dislocations leads to the generation of ISF and ESF, which eventually leads to phase transition and twins.

In Fig. 9 (a), the initial nucleation of a Shockley dislocation in variants 8($\text{Fe}_{0.1}\text{Co}_{0.5}\text{Ni}_{0.3}\text{Ti}_{0.1}$) is observed at a strain of 5.2 %, resulting in the formation of an ISF. As the strain increases to 6.1 %, crossed ISFs emerge owing to the nucleation and propagation of adjacent Shockley dislocations. This crossed ISF formation contributes to material strengthening and leads to secondary hardening, as depicted in Fig. 7 [41]. As the strain continues to increase, the prevalence of crossed ISFs intensifies, further enhancing the degree of secondary hardening. However, upon reaching a strain of 9 % (Fig. 9(c)), the crossed ISFs gradually disappear, resulting in a decline in stress. The ISFs transform from a crossed configuration to a parallel arrangement, with periodic spacing. This parallel ISF configuration contributes to the strengthening of HEAs [42] and accounts for the stress increase observed in Fig. 7.

Fig. 10 depicts the tensile deformation process of the variants 11 ($\text{Fe}_{0.1}\text{Co}_{0.4}\text{Ni}_{0.4}\text{Ti}_{0.1}$). This variant exhibits a unique deformation mechanism. At a strain of 4.2 % (Fig. 10(a)), Shockley dislocations and a significant number of disordered atoms emerge, some of which are located at the junction of ISFs and some are near vacancy defects. As the strain increases, these disordered atoms undergo a transformation into a BCC phase, and some of the ISFs transform into ESFs, as shown in Fig. 10 (b). Upon reaching a strain of 6.6 % (Fig. 10(c)), the ISFs and ESFs disappear, and nearly all the FCC phases transition into BCC phases,

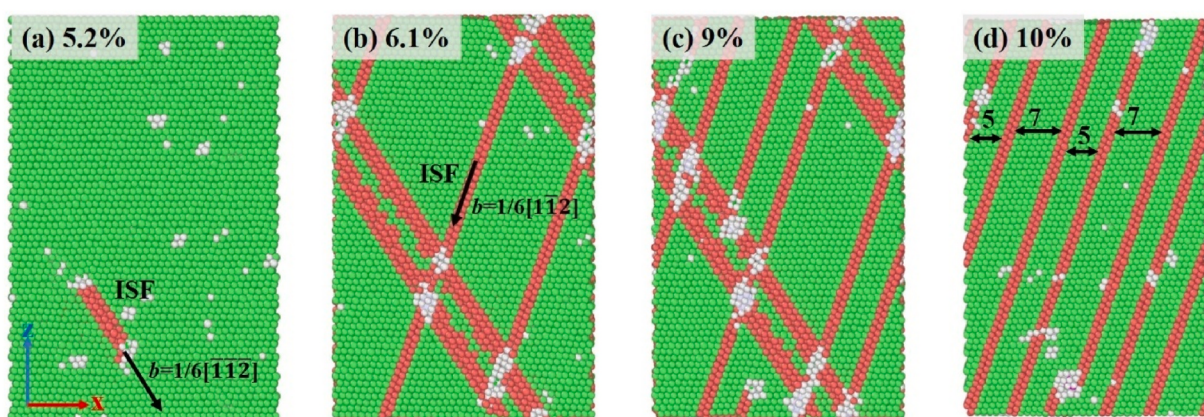


Fig. 9. Tensile deformation process of $\text{Fe}_{0.1}\text{Co}_{0.5}\text{Ni}_{0.3}\text{Ti}_{0.1}$ HEA. Shown at different strain levels: (a) 5.2 %, (b) 6.1 %, (c) 9 %, and (d) 10 %. The orientations of the x, y, and z axes correspond to $[112]$, $[1\bar{1}0]$, and $[1\bar{1}1]$, respectively.

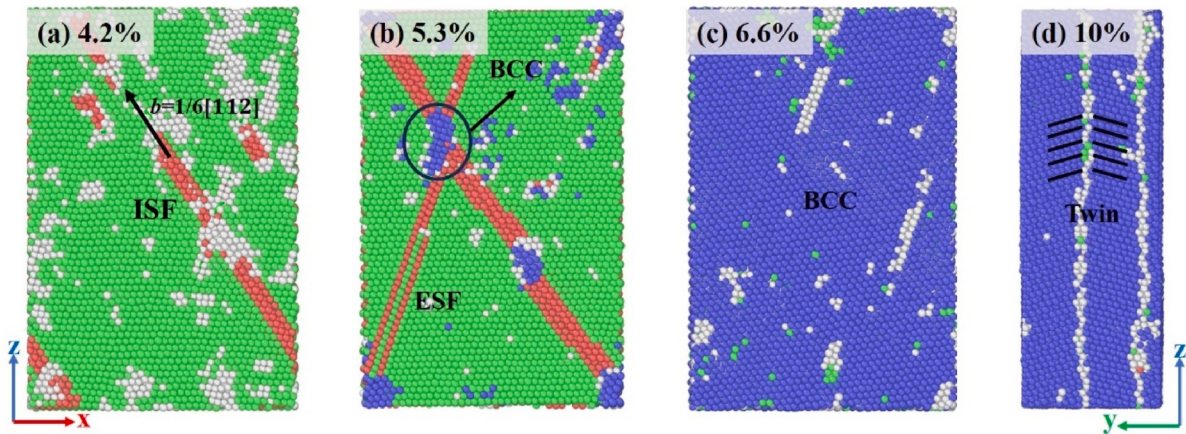


Fig. 10. Tensile deformation process of $\text{Fe}_{0.1}\text{Co}_{0.4}\text{Ni}_{0.4}\text{Ti}_{0.1}$ HEA. The strain levels are (a) 4.2 %, (b) 5.3 %, (c) 6.6 %, and (d) 10 %. The orientations of the x, y, and z axes are [112], [$\bar{1}10$], and [$\bar{1}\bar{1}1$], respectively.

indicating a martensitic phase transition that induces a TRIP effect. This transformation strengthens the HEA [43]. As the strain continues to increase, twin crystals appear. At this stage, the deformation mechanism shifts to a combination of TWIP and TRIP, further strengthening the alloy while maintaining high plasticity. Nevertheless, owing to its low yield point, this composition still exhibits a strength gap when compared to variant 15($\text{Fe}_{0.05}\text{Co}_{0.4}\text{Ni}_{0.5}\text{Ti}_{0.05}$) (refer to Table 3). Hence, it may not be structurally optimal. This means that under this component, the model we constructed is not a stable FCC phase, but a metastable state. With the further increase of stress, the precursor is transformed into BCC phase, and the constrained martensitic transformation occurs. Then, with the increase of stress, the deformation twins are produced. However, under this tensile condition, the strength of the alloy is not so good, but the plasticity is excellent.

Fig. 11 illustrates the tensile deformation process of the variant 15($\text{Fe}_{0.05}\text{Co}_{0.4}\text{Ni}_{0.5}\text{Ti}_{0.05}$), which exhibited the best performance, as discussed in the preceding sections. In Fig. 11(a), at a strain of 6.3 %, a Lomer–Cottrell dislocation forms in conjunction with appearance of ISFs owing to the motion of Shockley dislocations. Dislocation-driven mechanisms dominate plastic deformation, and with increasing strain, the ISFs gradually transform into ESFs. Notably, the Lomer–Cottrell dislocation lock remains stationary, contributing to the overall strength of the material [44].

Fig. 11(c) presents the response as the strain increases to 8 %. At this point, a portion of the ISF phases begins to undergo a transformation into the HCP phase. This is the reason the Shockley dislocation, as depicted in Fig. 8, is associated with a decrease in the growth of the HCP

structure. Meanwhile, the Lomer–Cottrell dislocation lock remains unaltered, ensuring the TRIP effect contributes to increased plasticity and high strength. Upon reaching a strain of 10 %, as the HCP phase ratio continues to rise, a new Lomer–Cottrell lock (blue area) forms simultaneously, as displayed in Fig. 11 (c). However, as the strain is insufficient for ESFs to transform into twins, no TWIP effect is observed. In summary, variant 15 ($\text{Fe}_{0.05}\text{Co}_{0.4}\text{Ni}_{0.5}\text{Ti}_{0.05}$) exhibits outstanding comprehensive properties and holds the potential for extensive utilization as a coating material and wear-resistant material in various sectors, including aerospace and automotive applications.

4. Conclusion

The effects of the chemical composition of FeCoNiTi HEAs on the lattice constant, elastic modulus, GSFE, and plastic deformation mechanism were systematically investigated using MD simulations. To identify the optimal variant exhibiting both high strength and plasticity, a new screening criterion was developed based on two key factors, namely (1) the shear modulus G and (2) the ISF energy γ_{ISF} . MC + MD calculations can be performed based on the optimized components in this article to further predict whether the effective components will form long-range and short-range ordering, and characterized by high-resolution transmission electron microscopy. The following conclusions were drawn from the screening criterion and simulation results:

- (a) Increasing the Ni and Co content while decreasing the Fe and Ti content leads a reduction in the lattice constant and an increase in

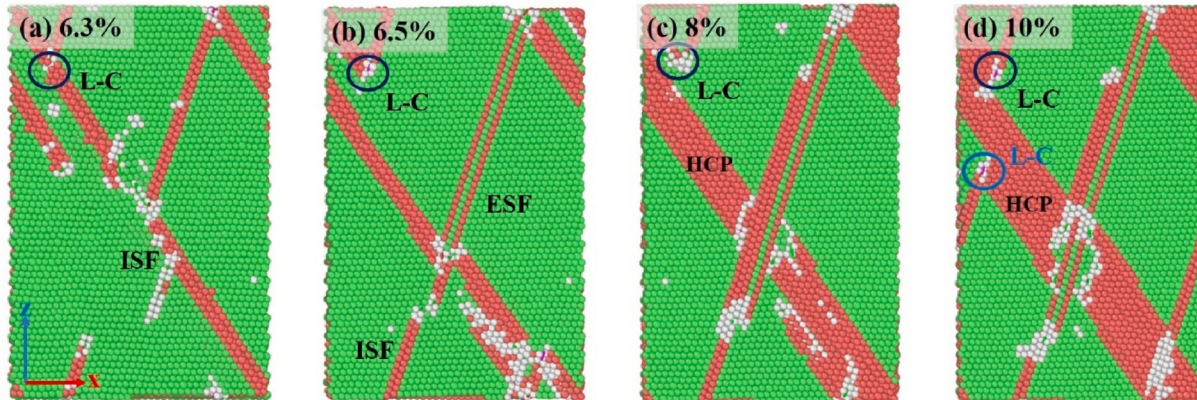


Fig. 11. Tensile deformation process of $\text{Fe}_{0.05}\text{Co}_{0.4}\text{Ni}_{0.5}\text{Ti}_{0.05}$ HEA at various strain levels: (a) 4.2 %, (b) 5.3 %, (c) 6.6 %, and (d) 10 %. The orientations of the x, y, and z axes are [112], [$\bar{1}10$], and [$\bar{1}\bar{1}1$], respectively.

- G. Higher Co content results in a slight decrease in C_P and v , contributing to a slight increase in plasticity while maintaining high strength.
- (b) As Co content increases and Fe and Ti content decreases, γ_{ISF} decreases. With an increase in Ni content and a reduction in Fe and Ti content, γ_{ISF} initially increases and then decreases. Consequently, higher Ni and Co content, along with lower Fe and Ti content, enhance the plasticity of FeCoNiTi HEAs.
 - (c) Five content groups meeting the criteria were selected, and tensile tests of these variants revealed that variant 15, $Fe_{0.05}Co_{0.4}Ni_{0.5}Ti_{0.05}$ HEA, exhibited the best combination of strength and plasticity. Notably, variant 11, $Fe_{0.1}Co_{0.4}Ni_{0.4}Ti_{0.1}$ HEA, underwent a martensitic transformation during the tensile process and generated deformation twins, contributing to TRIP and TWIP effects.
 - (d) The plastic deformation mechanisms predominantly entailed ISFs, ESFs, FCC→HCP phase transitions, FCC→BCC phase transitions, deformation twins, and Lomer–Cottrell dislocation locks. These mechanisms evolved with increasing strain, resulting in a continuous strengthening effect on HEAs.

Declaration of competing interest

The authors declare that they have no known competing financial interests or personal relationships that could have appeared to influence the work reported in this paper.

Acknowledgments

This project is financially supported by Major Science and Technology Project of Gansu Province (22ZD6GA008), the National Natural Science Foundation of China (52061025), Natural Science Foundation of Gansu Province (23JRRA820), Natural Science Foundation of Henan Province (232300421212), Basic research plan of key scientific research projects of Henan universities (22A430027), Scientific and technological breakthroughs in Henan Province (222102240068), Excellent Postgraduate Innovation Star Project of Gansu Province (2023CXZCZ-399), Local Science and Technology Development Fund Projects Guided by the Central Government, China (23ZYQB300).

References

- [1] George EP, Raabe D, Ritchie RO. High-entropy alloys. *Nat Rev Mater* 2019;4(8): 515–34.
- [2] Varvenne C, Luque A, Curtin WA. Theory of strengthening in fcc high entropy alloys. *Acta Mater* 2016;118:164–76.
- [3] Liu F, Liaw P, Zhang Y. Recent progress with BCC-structured high-entropy alloys. *J. Metals* 2022;12(3):501.
- [4] Zhao YJ, Qiao JW, Ma SG, et al. A hexagonal close-packed high-entropy alloy: the effect of entropy. *Mater Des* 2016;96:10–5.
- [5] Wang J, Jiang F, Wang L, et al. Cr addition-mediated simultaneous achievement of excellent strength and plasticity in non-equiautomic Nb-Ti-Zr-Ta-base refractory high-entropy alloys. *J Alloys Compd* 2023;946:169423.
- [6] Xu H, Zhang ZJ, Zhang P, et al. The synchronous improvement of strength and plasticity (SISP) in new Ni-Co based disc superalloys by controlling stacking fault energy. *Sci Rep* 2017;7(1):8046.
- [7] Laplanche G, Horst O, Otto F, et al. Microstructural evolution of a CoCrFeMnNi high-entropy alloy after swaging and annealing. *J Alloys Compd* 2015;647:548–57.
- [8] Han ZD, Luan HW, Liu X, et al. Microstructures and mechanical properties of TiNbMoTaW refractory high-entropy alloys. *Mater Sci Eng* 2018;712:380–5.
- [9] Tong Y-G, Tian N, Huang H-F, et al. Microstructure and deformation mechanism of dual-phase Al0.5CoCrNiFe high-entropy alloy[J]. *Rare Met* 2023;42(6):2020–7.
- [10] Jumaev E, Hong SH, Kim JT, et al. Chemical evolution-induced strengthening on AlCoCrNi dual-phase high-entropy alloy with high specific strength. *J Alloys Compd* 2019;777:828–34.
- [11] Watanabe A, Yamamoto T, Takigawa Y. Tensile strength of nanocrystalline FeCoNi medium-entropy alloy fabricated using electrodeposition. *Sci Rep* 2022;12(1): 12076.
- [12] Chen Y, Deng HW, Xie ZM, et al. Tailoring microstructures and tensile properties of a precipitation-strengthened (FeCoNi)94Ti6 medium-entropy alloy. *J Alloys Compd* 2020;828:154457.
- [13] Liu Y, Kang X, Jian T, Can H, Wei W, et al. Microstructure evolution and strength–ductility behavior of FeCoNiTi high-entropy alloy. *Chin J Mater Res* 2020;34(7): 535–44.
- [14] Ding ZY, He QF, Wang Q, et al. Superb strength and high plasticity in laves phase rich eutectic medium-entropy-alloy nanocomposites. *Int J Plast* 2018;106:57–72.
- [15] Raturi A, Aditya CJ, Gurao NP, et al. ICME approach to explore equiautomic and non-equiautomic single phase BCC refractory high entropy alloys. *J Alloys Compd* 2019;806:587–95.
- [16] Jo YH, Choi W-M, Sohn SS, et al. Role of brittle sigma phase in cryogenic-temperature-strength improvement of non-equi-atomic Fe-rich VCrMnFeCoNi high entropy alloys. *Mater Sci Eng* 2018;724:403–10.
- [17] Leong Z, Ramamurti U, Tan TL. Microstructural and compositional design principles for Mo-V-Nb-Ti-Zr multi-principal element alloys: a high-throughput first-principles study. *Acta Mater* 2021;213:116958.
- [18] Borovikov VV, Mendelev MI, Smith TM, et al. Molecular dynamics simulation of twin nucleation and growth in Ni-based superalloys. *Int J Plast* 2023;166:103645.
- [19] Qiao L, Liu Y, Zhu J. A focused review on machine learning aided high-throughput methods in high entropy alloy. *J Alloys Compd* 2021;877:160295.
- [20] Yang X, Li W, Fu Y, et al. Finite element modelling for temperature, stresses and strains calculation in linear friction welding of TB9 titanium alloy. *J Mater Res Technol* 2019;8(5):4797–818.
- [21] Rao SI, Woodward C, Parthasarathy TA, et al. Atomistic simulations of dislocation behavior in a model FCC multicomponent concentrated solid solution alloy. *Acta Mater* 2017;134:188–94.
- [22] Niu Y, Zhao D, Zhu B, et al. Investigations on the role of chemical short-range order in the tensile deformation of FCC Co30Fe16.67Ni36.67Ti16.67 high-entropy alloys via Monte Carlo and molecular dynamics hybrid simulations. *Comput Mater Sci* 2022;215:111787.
- [23] Rao SI, Varvenne C, Woodward C, et al. Atomistic simulations of dislocations in a model BCC multicomponent concentrated solid solution alloy. *Acta Mater* 2017; 125:311–20.
- [24] Jarlöv A, Ji W, Zhu Z, et al. Molecular dynamics study on the strengthening mechanisms of Cr–Fe–Co–Ni high-entropy alloys based on the generalized stacking fault energy. *J Alloys Compd* 2022;905:164137.
- [25] Branicio PS, Rino JP, Gan CK, et al. Interaction potential for indium phosphide: a molecular dynamics and first-principles study of the elastic constants, generalized stacking fault and surface energies. *J Phys Condens Matter* 2009;21(9):095002.
- [26] Qi Y, Zhao M, Feng M. Molecular simulation of microstructure evolution and plastic deformation of nanocrystalline CoCrFeMnNi high-entropy alloy under tension and compression. *J Alloys Compd* 2021;851:156923.
- [27] Khan TZ, Kirk T, Vazquez G, et al. Towards stacking fault energy engineering in FCC high entropy alloys. *Acta Mater* 2022;224:117472.
- [28] Haglund A, Koehler M, Catoor D, et al. Polycrystalline elastic moduli of a high-entropy alloy at cryogenic temperatures. *Intermetallics* 2015;58:62–4.
- [29] Thompson AP, Aktulga HM, Berger R, et al. Lammps - a flexible simulation tool for particle-based materials modeling at the atomic, meso, and continuum scales. *Comput Phys Commun* 2022;271:108171.
- [30] Zhou XW, Johnson RA, Wadley HNG. Misfit-energy-increasing dislocations in vapor-deposited CoFe/NiFe multilayers. *Phys Rev B* 2004;69(14):144113.
- [31] Yang Q, Hu Y, Zuo J-M. The dislocation structure of slip bands in deformed high entropy alloy nanopillars. *J Mater Sci Technol* 2021;95:136–44.
- [32] Nabizada A, Zarei-Hanzaki A, Abedi HR, et al. The high temperature mechanical properties and the correlated microstructure/textture evolutions of a TWIP high entropy alloy. *Mater Sci Eng* 2021;802:140600.
- [33] Bahramyan M, Mousavian RT, Brabazon D. Study of the plastic deformation mechanism of TRIP–TWIP high entropy alloys at the atomic level. *Int J Plast* 2020; 127:102649.
- [34] Liu SF, Wu Y, Wang HT, et al. Stacking fault energy of face-centered-cubic high entropy alloys. *Intermetallics* 2018;93:269–73.
- [35] Dodaran MS, Guo S, Khonsari MM, et al. A theoretical calculation of stacking fault energy of Ni alloys: the effects of temperature and composition. *Comput Mater Sci* 2021;191:110326.
- [36] Tanaka M, Yamasaki S, Morikawa T. Temperature dependence of the yield stress in TiZrNbHfTa body-centred cubic high-entropy alloy. *Mater Sci Eng* 2023;871: 144917.
- [37] Li L, Fang Q, Li J, et al. Lattice-distortion dependent yield strength in high entropy alloys. *Mater Sci Eng* 2020;784:139323.
- [38] Zuo L, Humber M, Esling C. Elastic properties of polycrystals in the Voigt-Reuss-Hill approximation. *J Appl Crystallogr* 1992;25(6):751–5.
- [39] Gao T, Song H, Wang B, et al. Molecular dynamics simulations of tensile response for FeNiCrCoCu high-entropy alloy with voids. *Int J Mech Sci* 2023;237:107800.
- [40] Zhang L, Qian K, Huang J, et al. Molecular dynamics simulation and machine learning of mechanical response in non-equiautomic FeCrNiCoMn high-entropy alloy. *J Mater Res Technol* 2021;13:2043–54.
- [41] Yang R, Yang L, Wang T, et al. Ultra-fine-grained equiautomic CoCrNi medium-entropy alloys with high density stacking faults and strengthening mechanisms. *Mater Sci Eng* 2023;870:144880.
- [42] Jian WW, Cheng GM, Xu WZ, et al. Physics and model of strengthening by parallel stacking faults. *Appl Phys Lett* 2013;103(13):133108.
- [43] Bae JW, Seol JB, Moon J, et al. Exceptional phase-transformation strengthening of ferrous medium-entropy alloys at cryogenic temperatures. *Acta Mater* 2018;161: 388–99.
- [44] Yan Z, Lin Y. Lomer–Cottrell locks with multiple stair-rod dislocations in a nanostructured Al alloy processed by severe plastic deformation. *Mater Sci Eng* 2019;747:177–84.